Pressure-Controlled Nanopipette Sensing in the Asymmetric-Conductivity Configuration

Sebastian A. Skaanvik[1], Xinyu Zhang[2], Ian J. McPherson[3], Yuqing Wang[1], Anne-Kathrine K. Larsen[1], Steffan M. Sønderskov[1], Patrick R. Unwin[4], Tomaso Zambelli[2], Mingdong Dong[1]*

(1) Interdisciplinary Nanoscience Center (iNANO), Aarhus University, 8000 Aarhus C, Denmark.
(2) Institute for Biomedical Engineering, Laboratory of Biosensors and Bioelectronics, ETH Zurich, Gloriastrasse 37, CH-8092 Zurich, Switzerland.
(3) Department of Chemistry, Loughborough University, Loughborough LE11 3TU, U.K.
(4) Department of Chemistry, University of Warwick, Coventry CV4 7AL, U.K.

*dong@inano.au.dk

Keywords: nanopipette, scanning ion conductance microscopy, scanning probe microscopy, surface charge mapping, electroosmotic flow, electromigration

Abstract

Nanopipettes are important tools across diverse disciplines including biology, physics, materials science, and electrochemistry, and precisely adjusting their characteristics is vital for many applications. Recent progress in this endeavor has involved using the asymmetric-conductivity configuration with different electrolyte solutions inside and outside of the nanopipette, which can greatly improve nanopipette sensing. However, understanding such measurements is challenging due to the complex interplay between diffusion, electromigration, and electroosmosis. Herein, we studied the simplified case of the asymmetric-conductivity configuration where classical ion current rectification due to ion-selective migration is minimized, while the effect of electroosmotic flow is maximized. We characterized the current-potential and current-distance relationship and revealed that this experimental configuration exhibits many of the characteristics of traditionally rectifying nanopipettes, such as surface charge sensitivity, while the current response can be understood simply from the rate and direction of solution mixing due to electroosmotic flow. To further improve the use of the asymmetric-conductivity configuration, a method was developed using external pressure to control the fluid flow rates at the aperture to tune the local ionic environment *in situ*, paving the way for novel, more reliable, and higher throughput nanopipette measurements.

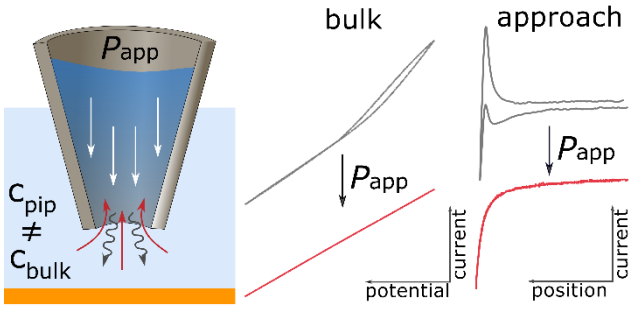

For ToC only

Introduction

Nanopipette sensing is a versatile approach that relies on glass capillaries that have been melted and pulled to a small aperture for highly sensitive electrical measurements to study single molecules,

materials, and living cells[1–5]. By precisely controlling the movement of the nanopipette, high-resolution mapping of physical properties like topography, stiffness, permeability, and surface charge is possible[6–12]. Moreover, nanopipettes are used to locally control extraction and delivery processes, including sampling/delivery to single cells and surface patterning[13–18]. In nanopipette measurements, a voltage is typically applied across two electrodes, placed inside and outside of the pipette. This generates a potential difference driving a resistance-limited ionic current through the pipette aperture. This ionic current is generally proportional to the ionic conductivity of the electrolyte and scaled by the geometry of the pipette, moreover, its modulation by interactions with an external surface or analyte is the sensing mechanism[19,20]. Nanopipettes exhibit complex current-voltage behavior where deviations from linear resistivity occur, a phenomenon commonly referred to as ion current rectification[21–23].

Ion current rectification in nanopipettes arises primarily from the surface charge of the pipette in low-to-moderate ion concentrations ($\leq$ 150 mM) and stems from the interplay between two main mechanisms, ion-selective migration, and electroosmotic flow. The surface charge of glass (borosilicate or quartz) pipettes is usually negative for pH > 4 resulting in an accumulation of cations within the electrical double layer at the pipette-electrolyte interface[24]. When the electrical double layer spans a substantial fraction of the pipette aperture, it alters the cation-to-anion migration ratio, leading to selective ion transport across it, mainly favoring cation migration. To maintain electroneutrality under this condition, concentration polarization results in ion accumulation and depletion on either side of the aperture. As a result, the total conductance increases at negative potentials (pipette electrode) and decreases at positive potentials, thereby increasing and decreasing the resulting current, respectively[25]. As the electrical double layer carries a net charge, it also moves under the influence of electric fields, dragging the surrounding solution with it from viscous friction, a phenomenon referred to as electroosmotic flow[26]. Electroosmotic flow disrupts the ion accumulation/depletion process, sometimes referred to as flow-induced rectification[27–30]. Moreover, whenever a nanopipette is positioned close to an external surface, surface-induced rectification is observed as the modulation of the ion accumulation/depletion and electroosmotic flow by the external surface further influences the rectification properties[11,31].

All these contributions result in a complex ion current rectification behavior that is dependent on the specific conditions. As ion current rectification has a profound influence on the sensing properties of nanopipettes, affecting noise, current magnitude, and analyte interactions[32,33], tuning it through experimental design is an important aspect of nanopipette use, and is typically achieved by tuning the electrolyte composition and pipette geometry and chemistry[34–40]. Alternatively, the ion current rectification can be tuned by using two different electrolyte solutions inside and outside of the pipette, herein referred to as the asymmetric-conductivity configuration[30,41,42]. Operation in the asymmetric-conductivity configuration has been shown to dramatically improve single-molecule detection in bulk and surface charge mapping[43,44]. This can be partially explained by the enhanced electroosmotic flow that occurs, but the mechanistic explanations for the rectification properties and improved sensing in many cases remain debated[45,46]. Additionally, sensing in the asymmetric-conductivity configuration is limited by the lack of ability to control local ion concentrations[27]. Hence, there is an urgent need for a better understanding of the asymmetric-conductivity configuration and improving its tunability.

Herein, the rectification properties of the asymmetric-conductivity configuration were elucidated when electroosmotic flow is active and mostly ascribed to the rapid, time-dependent mixing of the two different electrolyte solutions. The effect of this type of rectification on the current response in bulk and during surface interrogation was explored. Then, external pressure control was used to tune the properties of the asymmetric-conductivity configuration for *in-situ* controlled nanopipette

measurements (Figure 1). By imposing hydrodynamic flow with pressure (white arrows), the interplay between Fick's diffusion (grey arrows) and electroosmosis (red arrows) can be evaluated, and the ion concentration at the pipette aperture/sample finely tuned. Finite-element simulations were developed for quantitative evaluation of local flow velocities and concentration gradients. The introduced framework was found to provide novel advantages while shedding light on current nanopipette sensing and its potential future applications.

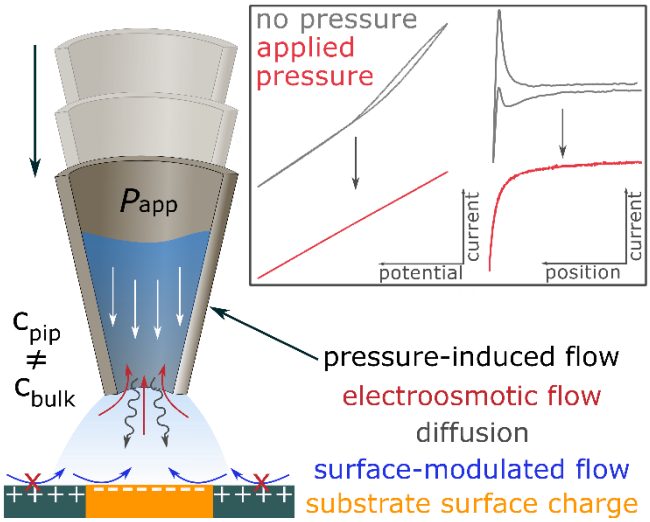

Figure 1: Scheme showing the mass-transport phenomena in the pressure-controlled nanopipette sensing framework based on the asymmetric-conductivity configuration (different conductivities in bulk and pipette). The shades of color indicate the ionic conductivity, where darker blue has higher ionic conductivity, and that of the bulk is white for simplicity. Pressure is used to generate a fluid flow that competes with the electroosmotic flow and diffusion. The plots in the grey box indicate the effect of pressure on current-potential and current-distance curves.

Results and Discussion

Ion Current Rectification in the Asymmetric-Conductivity Configuration

Under conventional circumstances, nanopipettes are made from quartz or borosilicate and carry a negative surface charge and are as a result "negatively" rectifying, *i.e.,* they have a higher conductance at negative pipette potentials (E) than at positive. In the asymmetric-conductivity configuration, the rectification properties are remarkably different such that a negatively charged pipette can even become positively rectifying[30,44,47]. This rectification behavior is related to the altered mass-transport from stronger spontaneous Fick's diffusion and electroosmotic flow that occurs in the asymmetric-conductivity configuration but is not fully understood in the context of nanopipette sensing. To improve our understanding of the asymmetric-conductivity configuration and help rationalize experimental nanopipette data, the role of conductivity differences between the pipette and bulk solutions on the ion current rectification was studied experimentally and supported by finite-element simulations. Using large nanopipettes, approximately 250 nm radius, relatively high flow rates can be achieved such that the contributions from electroosmotic flow can be assessed while the contribution from classical rectification is minimized.

First, current (*i*)-E sweeps were performed in KCl by varying the bulk concentration (c_{bulk}) while maintaining the pipette concentration (c_{pip}) constant at 150 mM. The concentration difference is

conveniently expressed by defining a dilution factor, R_{dil}, as the ratio of the pipette to the bulk concentration:

$$R_{\mathrm{dil}} = \frac{c_{\mathrm{pip}}}{c_{\mathrm{bulk}}}$$

Equation 1

The resulting *i-E* curves for R_{dil} = 5 and 0.5 compared with R_{dil} = 1, show dramatically different curves, demonstrating that the pipette behavior is not simply determined by the pipette solution, despite that almost all the resistance contribution of the system is expected to be from this region (Figure 2A). When the conductivity is modulated by increasing the viscosity with glycerol while maintaining the KCl concentrations the same, similar results are obtained, showing that these effects are the results of differences in ionic conductivity and that the ion current rectification may be modulated by controlling the viscosity, as opposed to the ion concentration (Supporting Information, Figure S1). The degree of ion current rectification can be associated with a rectification factor, R_{rect}, defined according to:

$$R_{\mathrm{rect}} = \frac{-i_{-750\ \mathrm{mV}}}{i_{+750\ \mathrm{mV}}}$$

Equation 2

R_{rect} is shown in Figure 2B for different R_{dil}, clearly demonstrating its high dependence on R_{dil} with positive rectification (R_{rect} > 1) seen at R_{dil} < 1, when the pipette solution is less conductive than the bulk solution. At R_{dil} = 1, R_{rect} = 0.99, demonstrating minimal classical rectification due to ion-selective transport.

A strong current hysteresis can be noticed, especially at positive potentials, for both R_{dil} with inverted direction, which is directly associated with the imposed concentration difference (up to 10% of the current value). The hysteresis is described according to the separation of forward and backward current traces at the same potential given by the following equation (Figure 2C, Supporting Information, Section S2):

$$R_{\mathrm{hyst}} = \frac{i_{\mathrm{forward}}\ (E)}{i_{\mathrm{backward}}\ (E)}$$

Equation 3

The time dependence of the *i-E* curves can also be demonstrated by a scan rate analysis, where the potential sweep rate is altered[27]. The effect of scan rate is more prominent at positive potentials than at negative, where an increase in current is seen with slower scan rates (Figure 2D). The *i-E* curves do not overlap for different potential sweep rates but do so for cycles at the same sweep rate (Supporting Information, Figure S3). Moreover, when the pipette surface charge is intentionally modified to be positive by poly-L-lysine (PLL) modification, the rectification and hysteresis behavior is flipped with respect to potential, showing that the rectification arises from the pipette surface charge and therefore the direction of the electroosmotic flow, as rectification from selective ion transport is not dominating for this pipette size (Supporting Information, Figure S4). All results are indicative of solution mixing by electroosmotic flow playing a central role in the observed ion current rectification in the studied system, and that a thorough characterization of this behavior is needed.

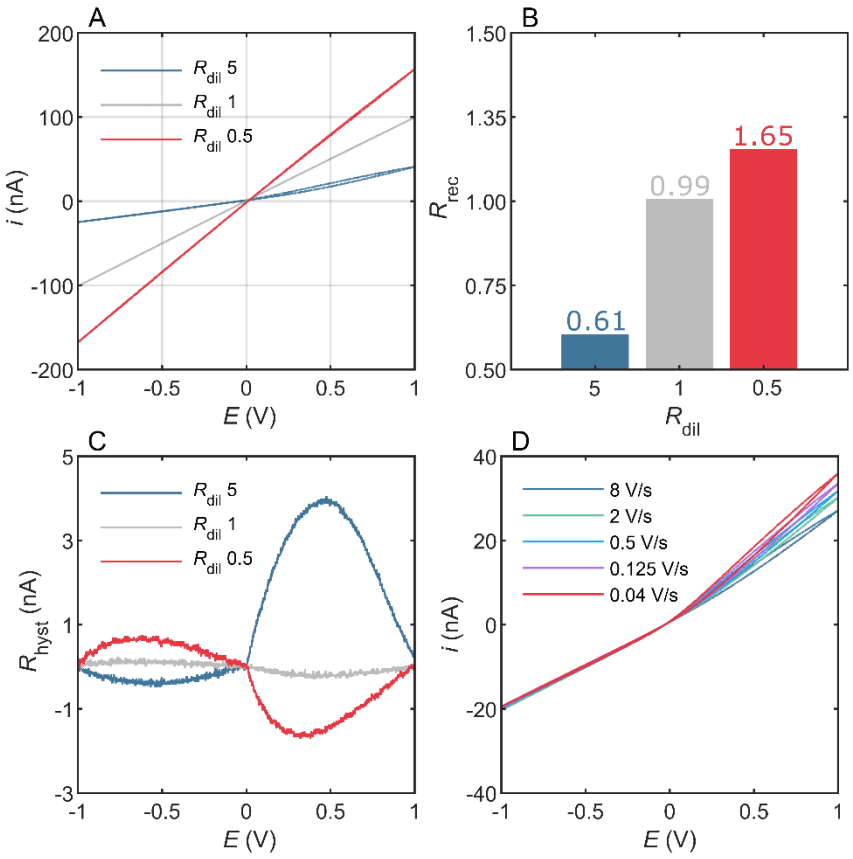

Figure 2: A) *i-E* curves for different R_{dil}. Conditions: c_{pip} = 150 mM KCl, scan rate of 4 V/s, and r_{pip} was estimated to be approximately 250 nm (evaluated by comparison to simulations). B) R_{rect} calculated from the curves in (A). C) R_{hyst} versus *E,* calculated from the curves from (A). D) Scan rate analysis for R_{dil} = 3 and r_{pip} of approximately 250 nm.

To describe these behaviors more quantitively and to rationalize the stronger time-dependence at positive potentials, a simulation model was built based on previous work including electroosmotic flow in the evaluation of the nanopipette response, which incorporates the Poisson, Nernst-Plank, and Navier-Stokes equations and the nanopipette geometry (Figure 3A)[23,48,49]. A nanopipette with an inner cone angle of 3˚, an intermediate value for borosilicate pipettes[50] (Supporting Information, Figure S5), and different pipette radii (r_{pip}, 225, 250, and 275 nm) were chosen. The simulated curves for R_{dil} = 1 and r_{pip} = 250 nm agree well with the experimental data, and this size was therefore used for further analysis (Supporting Information, Figure S6). The simulated curves for different R_{dil} (Figure 3B), show a high degree of similarity to the experimental curves, little rectification for R_{dil} = 1, and similar rectification behavior for R_{dil} = 5 and 0.5. Moreover, hysteresis is seen in the simulated data (Supporting Information, Figure S7), demonstrating that the simulations capture the aspects of the experimental data.

From the simulations, we can evaluate the fluid flow velocity (v) across the aperture for different potentials (shown for 1 V and -1 V in Figure 3C). The v magnitude is greater across the aperture in the asymmetric-conductivity configuration for negative and positive potentials compared to that of the symmetric configuration, where the inwards and outwards flow velocities are similar independent of potential. When evaluating the ion concentrations across the aperture (shown for $c_{K+, mean}$) during the *i-E* curve (Figure 3D), the shape of the *i-E* curve in the asymmetric-conductivity configuration can be understood from the time and potential-dependent mixing between the bulk and pipette solution[27]. Based on this finding, we attribute the higher flow velocities into the pipette at negative potentials to

the lower average electrolyte concentrations experienced by the pipette aperture at negative potentials, which increases the electroosmotic flow velocites[28] (due to the larger electrical double layer). This explanation is also consistent with the more prominent time-dependence seen at positive potentials resulting from the lower electroosmotic flow, whereas at negative potentials steady-state (aperture saturated with bulk solution) is reached, even at a scan rate of 8 V/s.

The extent to which the ion current rectification is affected by the mixing of the pipette and bulk solution is dependent on the magnitude of the electroosmotic flow, and it would be reduced for the smallest pipettes[27,28,48] (e.g. 10 nm), as electroosmotic flow is hindered under such circumstances. However, we argue that the contributions from this type of rectification may play a central part even for much smaller pipettes than what has been explored so far, as electroosmotic flow is typically still present to some extent and its effect is exacerbated in the asymmetric-conductivity configuration. As a result, a stronger convolution with classical ion current rectification behavior is expected for intermediate pipette sizes and the rectification properties cannot be explained by conductivity differences alone, as pointed out previously[30,46]. As presented herein, the evaluation of the effect of solution mixing due to electroosmotic flow be achieved with a scan rate analysis and is evident from strong hysteresis.

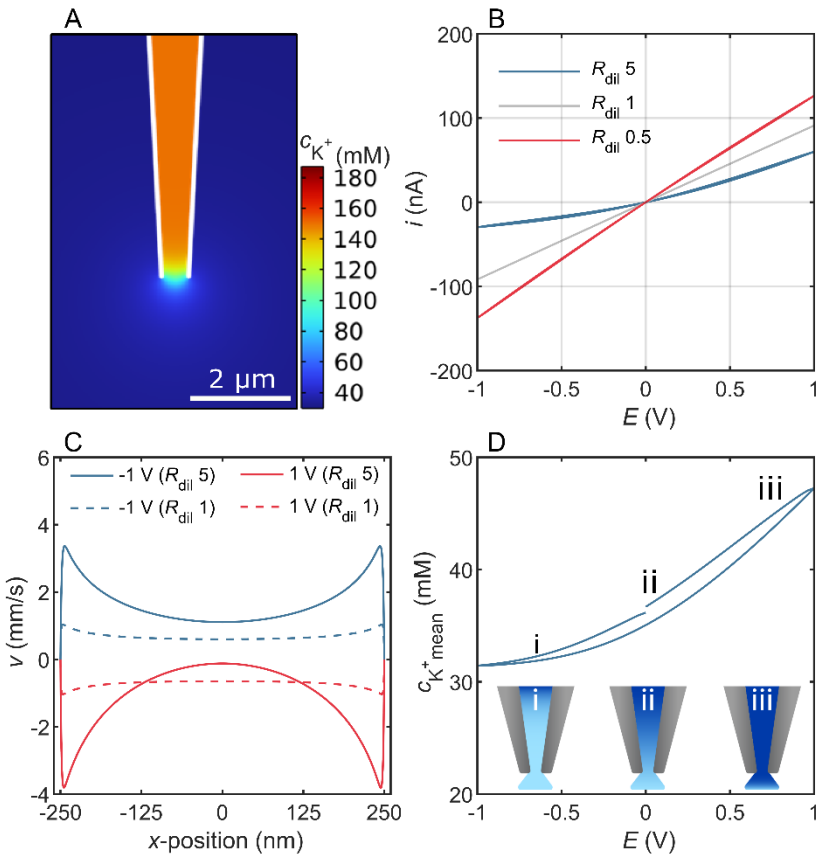

Figure 3: A) Simulation geometry overlaid with c_{K+} color plot. B) Simulated *i-E* curves for different R_{dil}, R_{pip} of 250 nm, and an inner half cone angle of 3˚. C) Evaluated v across the pipette aperture for different *E*, and R_{dil}. D) $c_{K+, mean}$ across the pipette aperture versus potential for an *i-E* sweep for R_{dil} = 5.

Pipette-Surface Interactions in the Asymmetric-Conductivity Configuration

A strong effect of R_{dil} on the *i-E* relationship has been shown in bulk, giving rise to enhanced rectification and hysteresis behavior. The role of this rectification and hysteresis towards the current-distance relationship may also show drastically altered characteristics, which has far-reaching implications for surface interrogations using nanopipettes. To better understand the pipette-surface interactions in the asymmetric-conductivity configuration, a series of approach-retract curves were carried out for varying R_{dil}, *E*, approach current thresholds, and approach/retract rates.

A strong current hysteresis is observed in the approach-retract curves in the asymmetric-conductivity configuration, more drastically for R_{dil} = 5 than for R_{dil} = 0.5, giving large current peaks during the approach and retraction, while current hysteresis is minimal at R_{dil} = 1 (Figure 4A). This effect is particularly strong for negative potentials, which suggests that this is a flow-driven process similar to what is seen in the bulk (Supporting Information, Figure S8). The current hysteresis in the approach curves is also modulated by viscosity when keeping the ion concentrations the same (Supporting Information, Figure S9). The inversion of the electroosmotic flow by PPL modification (to render the nanopipette walls positively charged) alters the pipette potential at which the current peaks happen, occurring only at positive potentials for a positively charged pipette, which means that this effect is strongest when the flow is directed into the pipette because of the higher flow velocities seen (for R_{dil} = 5), as previously explained from the lower conductivity in the aperture under such conditions (Supporting Information, Figure S10). Moreover, the hysteresis effect is also time-dependent similar to *i-E* measurements, and is consequently dependent on the approach rate and approach current thresholds (Supporting Information, Figure S11).

Understanding of the bulk *i-E* experiments is informative in explaining how electroosmotic flow is altered by the presence of the surface (Figure 4B). When the pipette is in bulk solution for $R_{dil} > 1$ and $E < 0$ V, strong electroosmotic flow, spontaneous Fick's diffusion, and electromigration are balanced such that the ionic concentration at the pipette aperture is close to that of the bulk (i). With the pipette moving closer to the surface, the electroosmotic flow remains almost unperturbed while the current diminishes because of the increasing resistance in the gap between the pipette and the surface (ii). As the pipette moves even closer to the surface, the electroosmotic flow becomes disrupted as the flow pathway is blocked such that the spontaneous Fick's diffusion dominates, increasing the concentration at the aperture: accordingly, the current augments, resulting in the small peak in the approach curve (iii). When the pipette is retracted and the effect of electroosmotic flow begins to be restored, the current peak in the retract curve is higher due to the temporary higher electrolyte concentration in the pipette induced by the approach curve (iv). Eventually, the current moves slowly back towards the approximate initial steady state (v). The results presented provide a simpler and clearer mechanistic understanding of previously reported current-enhancement effects, which have been shown to display the same time-dependence seen herein, for example, evident by a large difference between the approach versus the retract curve.[51]

One of the aspects regarding the modulation of the electroosmotic flow by the underlying surface is the role of its surface charge[52]. Hopping mode imaging was performed in the asymmetric-conductivity configuration over a charge-patterned surface to investigate if surface charge influences the current-distance relationship. Using a light-patterning strategy, a fibrinogen/polyethylene glycol (PEG) pattern was created where the fluorescently labeled fibrinogen can be seen in Figure 4C (Supporting Information, Figure S12). The fibrinogen carries a negative charge while the PEG layer has a neutral or low positive charge due to its cation-binding properties.[53,54] When the peak current in the retraction curve is evaluated with respect to the bulk current (evaluated at the beginning of each approach

curve), a clear contrast can be seen (Figure 4D). Higher current peaks are observed over the negatively charged fibrinogen regions (Figure 4E). This was also evaluated from independent experiments with circular features for identification (Supporting Information, Figure S13). This increase in the peak current can be understood as a greater shift in concentration occurring over a negatively charged surface due to a maintained electroosmotic flow pathway, most likely by allowing the nanopipette to move closer to the surface and therefore the concentration disruption to be more effective.

We characterized the current-distance relationship in the asymmetric-conductivity configuration and demonstrated a new type of nanopipette measurement where the rate of mixing between the nanopipette and the bulk is probed in a time-dependent manner, which is sensitive to the surface charge of the substrate. This type of mapping can be achieved with fairly large nanopipettes because electroosmotic flow is still active for such nanopipettes despite little classical ion current rectification. While the surface-induced rectification, pipette rectification, and hysteresis effects seen have already theoretical foundation in the symmetric-conductivity configuration[55–58], it is clearly demonstrated herein that these effects are exacerbated when concentration asymmetries exist. One important implication is that strict concentration symmetry is essential for reliable nanopipette measurements. Even in a freshly filled pipette, small concentration gradients may still be present, presumably from the dissociation of silanol groups considering that the pipette aperture is filled by capillary action.

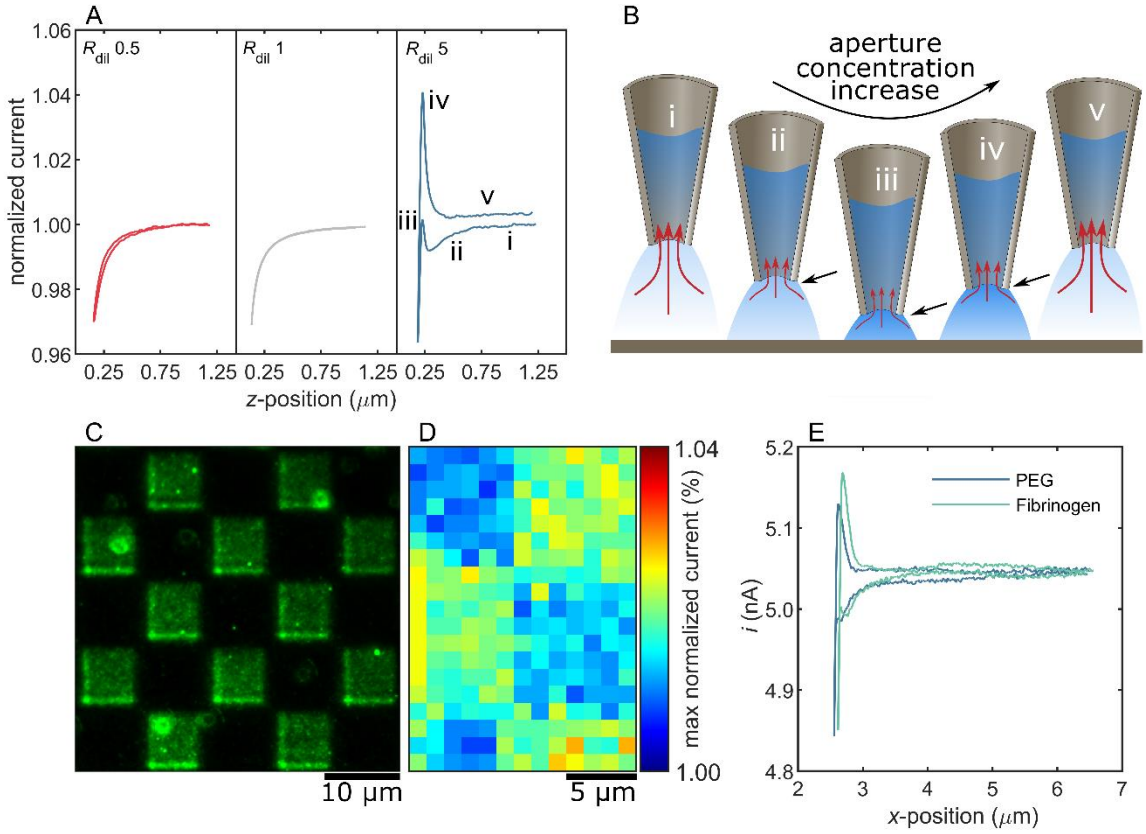

Figure 4: A) Approach curves in the asymmetric-conductivity configuration over a silicon wafer, where the current is normalized to the bulk. Conditions: E = -250 mV and approach/retract rate = 250 nm/s. B) Proposed mechanism for the strong hysteresis in the current-distance relationship seen in (A). C) Fluorescent imaging (GFP channel) of the micropatterned surface of Fibrinogen-Alexa488 (green, negative charge) on PEG-modified glass (black, neutral charge). D) Hysteresis map by evaluating the maximum current normalized to base current in bulk in the approach curve. E) Example approach-retraction curves over the PEG and fibrinogen regions. Conditions (D/E): E = -250 mV, R_{dil} = 5, and approach/retract rate = 4 um/s.

Tuning the Asymmetric-Conductivity Configuration using Pressure

While there are many advantages to using the asymmetric-conductivity configuration, the disadvantages are high-time dependence and limited ability to control the ionic environment at the pipette aperture. Relying on theoretical work about the effect of external pressure on the hydrodynamic flow induced inside a nanopipette[7,48,59,60], we explored the use of pressure in the asymmetric-conductivity configuration to be able to tune the local ion concentration and therefore sensing properties *in situ*.

The effect of external pressure in the asymmetric configuration for R_{dil} = 5 is shown in Figure 5A with the symmetric-conductivity configuration for the bulk and pipette concentrations shown for reference (30-30 and 150-150 mM KCl, respectively). When a positive or negative pressure (several mbar) is applied the *i-E* curves are shifted between the two extreme limiting cases, indicating that pressure can be indeed of advantage to tune the nanopipette properties by introducing fluid flow through the nanopipette. Steady-state is normally achieved after several seconds. By restraining the potential in the range of -25 to 25 mV, the pipette resistance (R_{pip}) in the absence of strong electroosmotic can be estimated. The use of pressure (-25 to 25 mbar) allows full control of the R_{pip} as demonstrated in Figure 5B, showing that the pressure needed to shift the concentration gradients is mostly pipette dependent, with slightly higher pressure needed to overcome the stronger diffusion at high R_{dil}. Similarly, the R_{rec} is controlled (Figure 5C). When 25 mbar pressure is applied, all current hysteresis is gone in the approach curves because pressure-induced flow counteracts the electroosmotic flow (Figure 5D). A schematic depiction of this process is shown in Figure 5E.

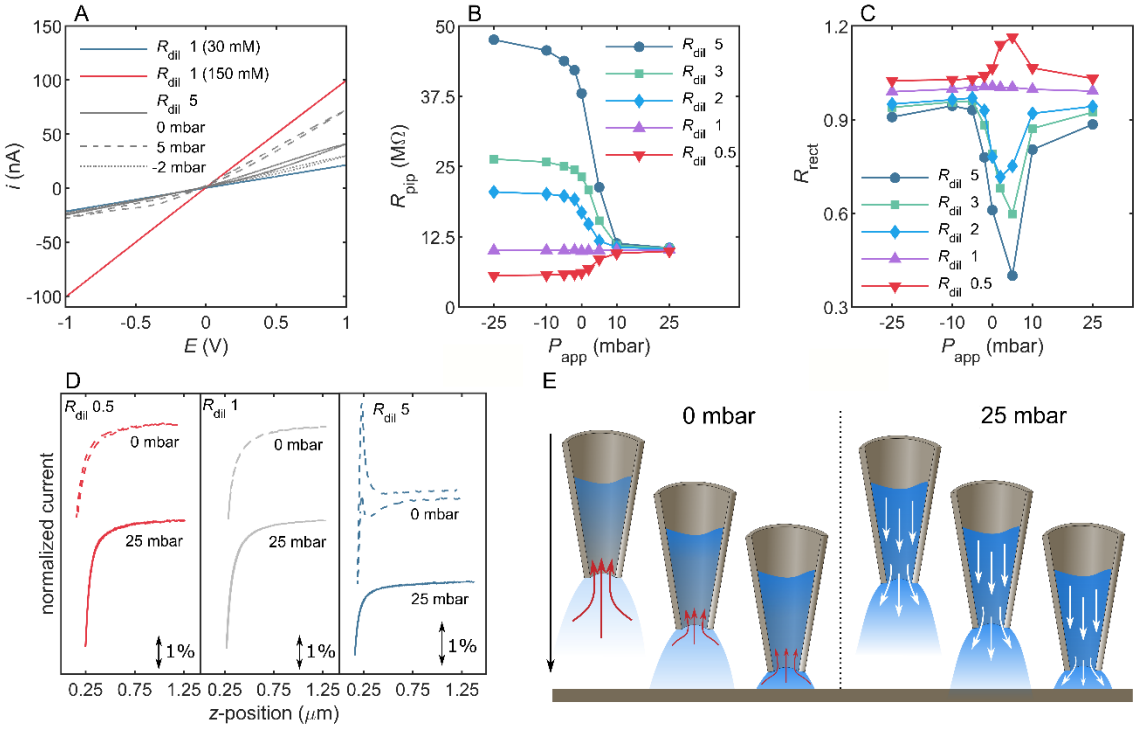

Figure 5: A) Effect of P_{app} on the *i-E* relationship for R_{dil} = 5, with the limiting cases for R_{dil} = 1 shown for reference (150 mM KCl (red line) and 30 mM KCl (blue line)). The r_{pip} was estimated to be 250 nm by comparison to simulated data. B-C) R_{pip}-P_{app} (B) and R_{rect}-P_{app} (C) relationship after equilibration (30 s after applying pressure). D) Approach-retract curves for varying R_{dil} with and without 25 mbar

external pressure applied. E) Scheme demonstrating the effect of pressure-induced flow counteracting the electroosmotic flow during an approach curve for $R_{dil} > 1$ and $E < 1$. In the absence of pressure, the disruption of electroosmotic flow (red arrows) by the presence of the surface results in an increase in ionic concentration at the aperture, increasing the measured current. When high positive pressure is applied to the pipette, pressure-induced flow dominates, which to a much lesser extent affected by the surface, and the pipette aperture remains saturated with pipette solution during the approach curve.

Quantitative interpretation of nanopipette measurements is essential to most applications. To better understand and determine the concentration and flow profiles under externally applied pressure, a simulation model was developed, incorporating pressure-induced flow, which matches well with the behavior of the experimental data (Figure 6A). The flow profile can then be evaluated across the aperture, showing fluid flow with a higher flow velocity at the aperture center (Supporting Information, Figure S14). v_{mean} across the aperture varies minimally, but linearly with the applied potential during an *i-E* sweep, meaning that the flow induced by pressure overcomes the electroosmotic flow, and ± 25 mbar can introduce flow velocities from approximately -10 mm s^{-1} to 10 mm s^{-1}, which are roughly linear with respect to the applied pressure (Figure 6B, Supporting Information Figure S14). The concentrations resulting from the pressure-induced flow are shown in Figure 6C, where the concentrations vary slightly during the *i-E* sweep, but this effect is reduced at higher pressures.

Our results show that externally applied pressure is an attractive means of tuning the flow velocities, and consequently the ion concentrations, at and close to the aperture. At the same time, the high degree of linearity in the systems makes the relationship between externally applied pressure and concentration relatively straightforward to interpolate across different potentials. It also has the advantage of being able to remove hysteresis effects when desired.

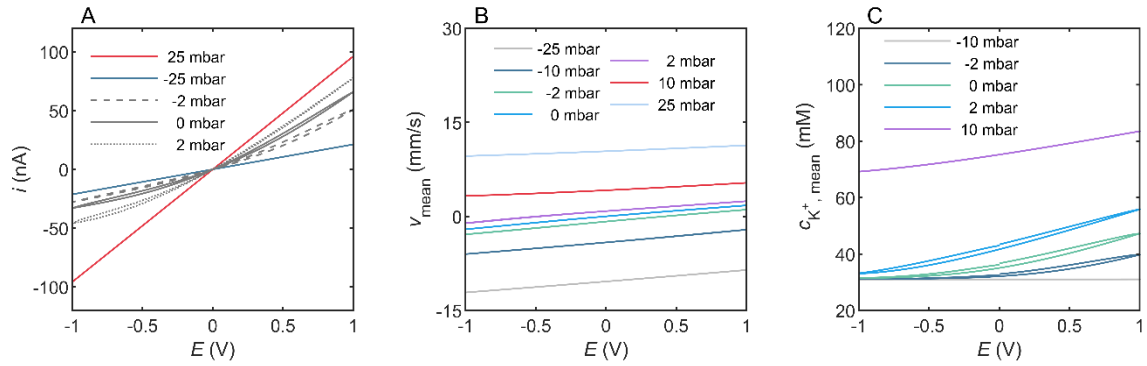

Figure 6: A) Simulated *i-E* curves for different P_{app}. Conditions: R_{dil} = 5, c_{pip} = 150 mM KCl, and r_{pip} = 250 nm. B) v_{mean} versus *E*, evaluated as the average flow velocity across the tip of the nanopipette orifice during an *i-E* sweep for different P_{app}. C) $c_{K+,\ mean}$ across the tip of the nanopipette aperture during an *i-E* sweep for different P_{app}.

Pressure-Controlled Constant-Current Imaging Using the Asymmetric-Conductivity Configuration

High-resolution imaging of physical properties is a core strength of nanopipette sensing, where topography and surface charge mapping have been carried out down to the single nanoparticle and (bio)molecular level[61,62]. While the hopping mode configuration is more commonly adopted due to its easier implementation and analysis, constant-current imaging in the direct current mode is an

attractive high-resolution surface charge mapping method, where the surface charge is manifested as topography distortions[6,61]. In this section, we explore constant-current imaging in the asymmetric-conductivity configuration and the possibility of tuning such imaging using external pressure.

A model system was chosen of multilayer MoS_2 sheets on (3-Aminopropyl)triethoxysilane (APTES)-treated mica, which should display a large surface charge contrast and reliable imaging due to mica's atomically smooth cleavage (Figure 7A). The high degree of contrast in surface charge allows the study of its effect on the modulation of the electroosmotic flow. A smaller pipette was used for imaging, with a radius estimated to be approximately 50 nm, and the *i-E* curve for this nanopipette is shown in Figure 7B for different P_{app}. At 5 mbar the measured current is approximately the midpoint between high positive and high negative pressures at the imaging potential of -100 mV and R_{dil} = 3, suggesting that the electroosmotic flow and pressure-induced flow is fairly balanced at this pressure (Supporting Information, Figure S15). Constant-current imaging was performed below, at, and above this pressure (0, 5, and 10 mbar, Figure7C-E), and the resulting line profiles are shown in Figure 7F. The data reveal an increased apparent height of the MoS_2 layer at 5 mbar (19.6 nm) versus 16.8 nm and 16.5 nm for 0 and 10 mbar, respectively. Moreover, there is a marked difference in imaging stability at 5 mbar compared to 0 and 10 mbar, which appears as a "noisy" topography profile.

The imaging instability seen at 5 mbar occurs when the concentration gradient across the pipette is high. This behavior can be understood by the effect of small fluctuations in the electrode potential difference due to noise, which will result in a change in the average ion concentration of the resistance-contributing volume at the pipette aperture, such that the resistance of the pipette is modulated by the noise. This effect is also noticed in bulk where the noise levels are dependent on pressure and applied potential (Supplementary Information, Figure S16). At 10 mbar the pressure-induced flow dominates such that the concentration gradient across the aperture becomes low, and to a much lesser degree is affected by noise. At 0 mbar, the electroosmotic flow into the aperture is strong, the pipette aperture is mostly saturated with the bulk solution, and small changes due to noise are not substantial enough to affect the concentration in the aperture, and therefore the current.

Surface-induced topography distortions occur in the symmetric-conductivity configuration due to surface charge heterogeneity, but this effect is evidently enhanced in the presence of concentration gradients and can be tuned with pressure. Within the framework herein, the electroosmotic flow velocity into the pipette is altered by the surface charge of the substrate, and the ionic concentrations respond accordingly, modulating the measured height. For example, the MoS_2 is more negatively charged than APTES-modified mica, and therefore the inward flow is increased when the pipette moves from mica to MoS_2 and the aperture concentration decreases, and the current decreases, which in turn increases the measured height (Figure 7G). The nanopipette does, however, show traditional rectification behavior in bulk (evaluated at high negative and positive pressures and shown in the Supporting Information, Figure S15). This system is, therefore, a powerful example of the convolution of mixing-driven rectification together with classical rectification in the use of smaller nanopipettes in the asymmetric-conductivity configuration, showing a dominating effect of electroosmotic flow.

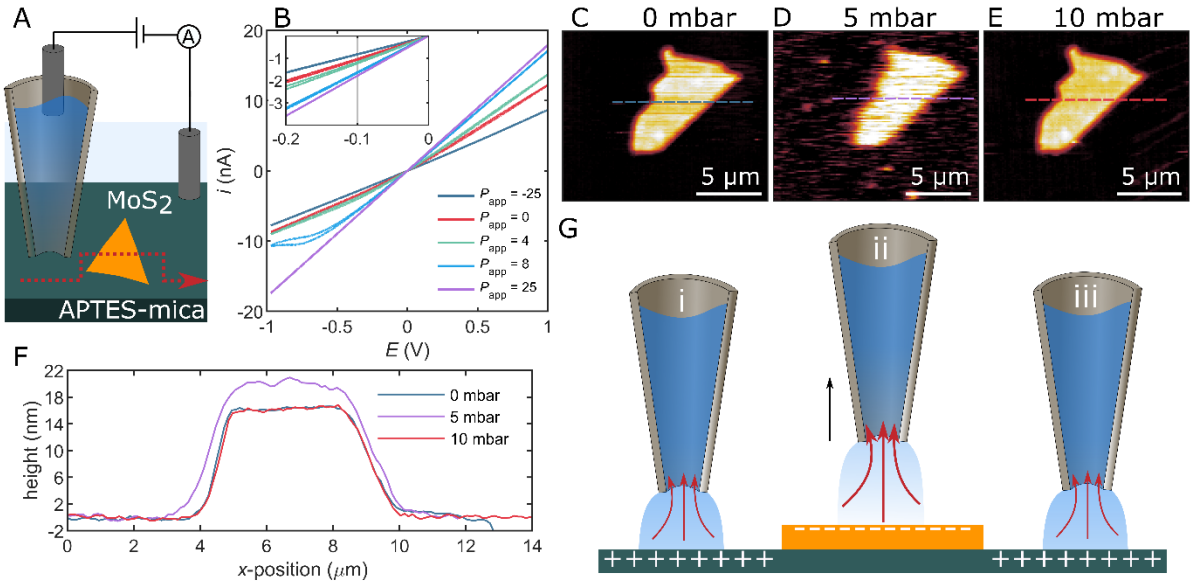

Figure 7: A) Schematic of constant-current imaging setup. B) *i-E* curves for different P_{app} for the nanopipette used for imaging (R_{dil} = 3, scan rate = 4 V/s, and r_{pip} estimated to be around 50 nm). C-E) Constant-current images of a multilayer MoS_2 sheet on APTES-treated mica in KCl in the asymmetric-conductivity configuration (98% current threshold and E = -100 mV). F) Center line profiles for the images in C-E. G) Schematic of the topography distortion effect seen at 5 mbar pressure, where over the positively charged APTES-treated mica, the electroosmotic flow is low, whereas, over the negatively charged MoS_2, electroosmotic flow is increased. This increase moves the solution of lower conductivity into the pipette, thereby lowering the current, and the nanopipette compensates by moving upwards, increasing the measured height of the multilayer MoS_2.

Conclusions

The asymmetric-conductivity configuration, using different electrolyte concentrations in the nanopipette and bulk, provides an additional dimension to improve the use and performance of nanopipettes by altering their properties. Herein, we studied the case of minimal classical rectification but strong electroosmotic flow by using larger pipettes than for conventional nanopipette sensing (a radius of 250 nm was used). We demonstrated that time-dependent solution mixing dominates the nanopipette current response in this system, a clear deviation from the traditional steady-state behavior of nanopipette in the symmetric-conductivity configuration and characterized this behavior in detail. This included tip-surface interactions, including the modulation of the electroosmotic flow by the surface charge of an underlying substrate, which had a pronounced effect on approach curves and constant-current imaging. One key finding in this regard is showing that surface charge mapping can be carried out with much larger nanopipettes when using the asymmetric-conductivity configuration, up to several µm, since electroosmotic flow is active for larger nanopipettes, compared to classical rectification. While the configuration studied herein is desirable in itself because the rationalization of the data is simply dictated by the change in direction of the electroosmotic flow, we also make the point that the solution mixing is a *contributing mechanism* to most nanopipette systems that rely on the asymmetric-conductivity configuration, including single-entity translocation sensing, even if the nanopipettes have a much smaller radius than 250 nm. In fact, in this work, strong flow-driven rectification was demonstrated for constant-current imaging with nanopipettes with a radius of approximately 50 nm. We have also introduced a new nanopipette sensing framework where external pressure is used to control the local ionic environment and flow velocity at the nanopipette

aperture. This allows for full control of nanopipette response *in situ* when using the asymmetric-conductivity configuration and opens up many possibilities for nanopipette applications, including rapid screening of different electrolytes, modulating the surface charge sensitivity, controlled delivery, and tuned single-entity translocation measurements.

Methods

Nanopipette measurements Nanopipette measurements were carried out using a Bio-XE SPM system (Park Systems, Korea) mounted on a Nikon Eclipse Ti microscope (Nikon, Japan). A DLPCA-200 current amplifier (FEMTO, Germany) was used for low-current measurements with an optional 10 kHz Bessel filter. Ag/AgCl electrodes were fabricated by immersion of silver wire (0.025 mm, Goodfellow, UK) in $FeCl_3$ for at least 30 min. The electrode potential differences were referenced with respect to the potential of zero current to account for the different electrode potentials from the asymmetric amount of chloride. Pressure was applied with a Cytosurge pressure controller (Cytosurge, Switzerland).

Nanopipette fabrication, modification, and characterization Nanopipettes were fabricated with a P-2000 F-type puller (Sutter instruments, US) and were fabricated from borosilicate capillaries (1.0/0.5 mm, Sutter instruments, US) with the following protocol: 330/330, 3/3 30/30, 220/220, 0/150 (small nanopipette, R_{pip} ≈ 50 nm) and 330/330 3/3 30/30 220/220 0/100 large nanopipettes (large nanopipettes, R_{pip} ≈ 250 nm). Pipette surface charge inversion was achieved by 5 min immersion in 0.01% PLL, followed by rigorous rinsing in ultrapure water (18.2 MΩcm). Pipette size was estimated by combining Hall's estimation of the access resistance and the expression for the resistance of a cone[63,64] assuming 8,480 µS cm^{-1} to be the conductivity of 50 mM KCl[27], and the inner cone angle to be 3˚.

Fibrinogen patterning Glass coverslips were rinsed with 96% EtOH, dried, and treated by glow discharge (25 mA, 45 s). PLL(20)-g(3.5)-PEG(2) (10 µL, 0.1 mg/mL in Phosphate buffered saline (PBS, Alvéole, France) was added to the sample and it was incubated for 30 min. Samples were rinsed thoroughly with PBS, dried, and 10 µL PLPP (Alvéole, France) was added. Light-induced patterning was performed using a PRIMO micropatterning device (Alvéole, France) mounted on an IX83 inverted widefield microscope (Olympus, Japan) using a 20x objective and a light dose of 800 mJ/mm^2. The Leonardo software was used to control the printing. After printing, samples were rinsed thoroughly with PBS and incubated with 50 µg/mL fibrinogen-A488 (Invitrogen, Massachusetts, USA). Samples were imaged using fluorescence microscopy using an IX83 inverted wide-field microscope.

MoS_2 synthesis and deposition on mica. The micromechanical cleavage technique was used to exfoliate layered bulk MoS_2 crystals into thin flakes. A polydimethylsiloxane (PDMS) stamp was used to transfer the MoS_2 from the tape to the PDMS stamp before depositing it on mica. Mica was modified with APTES by vapor deposition under reduced pressure for 60 min and dried under nitrogen.

Finite-element Simulations. Finite-element simulations were carried out using COMSOL Multiphysics version 6.1. The ion current, flow, and concentration profiles were simulated by numerical solution of the coupled Nernst-Planck, Poisson, and Navier-Stokes equations for the chosen nanopipette geometry. The nanopipette was modelled as a hollow cone with an inner cone angle of 3˚, a surface charge density of -5 mC/m^2, and different pipette radiuses depending on the specific conditions. A detailed description of simulation parameters and boundary conditions is given in the Supporting Information, Section S17. The COMSOL report is available as Supporting Information 2.

Acknowledgments

This research was supported by grants from the EU H2020 Marie Sklodowska-Curie Action SENTINEL no. 812398 and the Sino-Danish Center for Education and Research.

Conflict of Interest

The authors declare no conflict of interest.

Associated Content

Data Availability Statement

The data that support the findings of this study are openly available from the authors after request.

Supporting Information

The following files are available free of charge.

Supporting Information 1: Modulation of the Conductivity by Altering the Viscosity with Glycerol, Calculation of Current Hysteresis, Multiple Scans at the Same Scan Rate During Scan Rate Analysis, Effect of Pipette Charge on Ion Current Rectification and Current Hysteresis, Definition of Nanopipette Inner Cone Half Angle, Evaluation of Pipette Size by Comparison to Simulations, Current Hysteresis in Simulated Data, Effect of Pipette Potential on the Current Peak Magnitude, Glycerol Addition to Bulk for Constant Electrolyte Concentration, Effect of Pipette Charge on Current Hysteresis Peaks, Effect of Approach Parameters on Current Hysteresis Peaks, Fibrinogen patterning, Additional Information on Simulations with Externally Applied Pressure, and Bulk Behavior of Nanopipette Used for Constant-current Imaging

Supporting Information 2: COMSOL report with additional information on the finite-element simulations

References

(1) Morris, C. A.; Friedman, A. K.; Baker, L. A. Applications of Nanopipettes in the Analytical Sciences. *Analyst* **2010**, *135*, 2190–2202.

(2) Wang, Y.; Skaanvik, S. A.; Xiong, X.; Wang, S.; Dong, M. Scanning Probe Microscopy for Electrocatalysis. *Matter* **2021**, *4*, 3483–3514.

(3) Page, A.; Perry, D.; Unwin, P. R. Multifunctional Scanning Ion Conductance Microscopy. *Proc. R. Soc. A* **2017**, *473*, 20160889.

(4) Skaanvik, S. A.; Gateman, S. M. Probing Passivity of Corroding Metals Using Scanning Electrochemical Probe Microscopy. *Electrochem. Sci. Adv.* **2023**, e2300014.

(5) Lüchtefeld, I.; Pivkin, I. V; Gardini, L.; Zare-Eelanjegh, E.; Gäbelein, C.; Ihle, S. J.; Reichmuth, A. M.; Capitanio, M.; Martinac, B.; Zambelli, T.; Vassalli, M. Dissecting Cell Membrane Tension Dynamics and Its Effect on Piezo1-Mediated Cellular Mechanosensitivity Using Force-Controlled Nanopipettes. *Nat. Methods* **2024**, *21*, 1063–1073.

(6) Klausen, L. H.; Fuhs, T.; Dong, M. Mapping Surface Charge Density of Lipid Bilayers by Quantitative Surface Conductivity Microscopy. *Nat. Commun.* **2016**, *7*, 12447.

(7) Rheinlaender, J.; Schäffer, T. E. Mapping the Mechanical Stiffness of Live Cells with the Scanning Ion Conductance Microscope. *Soft Matter* **2013**, *9*, 3230–3236.

(8) Novak, P.; Li, C.; Shevchuk, A. I.; Stepanyan, R.; Caldwell, M.; Hughes, S.; Smart, T. G.; Gorelik, J.; Ostanin, V. P.; Lab, M. J.; Klenerman, D.; Korchev, Y. E. Nanoscale Live-Cell Imaging Using Hopping Probe Ion Conductance Microscopy. *Nat. Methods* **2009**, *6*, 279–281.

(9) McKelvey, K.; Kinnear, S. L.; Perry, D.; Momotenko, D.; Unwin, P. R. Surface Charge Mapping with a Nanopipette. *J. Am. Chem. Soc.* **2014**, *136*, 13735–13744.

(10) Paschoalino, W. J.; Payne, N. A.; Pessanha, T. M.; Gateman, S. M.; Kubota, L. T.; Mauzeroll, J. Charge Storage in Graphene Oxide: Impact of the Cation on Ion Permeability and Interfacial Capacitance. *Anal. Chem.* **2020**, *92*, 10300–10307.

(11) Sa, N.; Lan, W. J.; Shi, W.; Baker, L. A. Rectification of Ion Current in Nanopipettes by External Substrates. *ACS Nano* **2013**, *7*, 11272–11282.

(12) Rheinlaender, J.; Schäffer, T. E. Measuring the Shape, Stiffness, and Interface Tension of Droplets with the Scanning Ion Conductance Microscope. *ACS Nano* **2024**, *18*, 16257–16264.

(13) Momotenko, D.; Page, A.; Adobes-Vidal, M.; Unwin, P. R. Write-Read 3D Patterning with a Dual-Channel Nanopipette. *ACS Nano* **2016**, *10*, 8871–8878.

(14) Babakinejad, B.; Jönsson, P.; López Córdoba, A.; Actis, P.; Novak, P.; Takahashi, Y.; Shevchuk, A.; Anand, U.; Anand, P.; Drews, A.; Ferrer-Montiel, A.; Klenerman, D.; Korchev, Y. E. Local Delivery of Molecules from a Nanopipette for Quantitative Receptor Mapping on Live Cells. *Anal. Chem.* **2013**, *85*, 9333–9342.

(15) Hennig, S.; Van De Linde, S.; Bergmann, S.; Huser, T.; Sauer, M. Quantitative Super-Resolution Microscopy of Nanopipette-Deposited Fluorescent Patterns. *ACS Nano* **2015**, *9*, 8122–8130.

(16) Page, A.; Kang, M.; Armitstead, A.; Perry, D.; Unwin, P. R. Quantitative Visualization of Molecular Delivery and Uptake at Living Cells with Self-Referencing Scanning Ion Conductance Microscopy-Scanning Electrochemical Microscopy. *Anal. Chem.* **2017**, *89*, 3021–3028.

(17) Nadappuram, B. P.; Cadinu, P.; Barik, A.; Ainscough, A. J.; Devine, M. J.; Kang, M.; Gonzalez-Garcia, J.; Kittler, J. T.; Willison, K. R.; Vilar, R.; Actis, P.; Wojciak-Stothard, B.; Oh, S. H.; Ivanov, A. P.; Edel, J. B. Nanoscale Tweezers for Single-Cell Biopsies. *Nat. Nanotechnol.* **2019**, *14*, 80–88.

(18) Chau, C. C.; Maffeo, C. M.; Aksimentiev, A.; Radford, S. E.; Hewitt, E. W.; Actis, P. Single Molecule Delivery into Living Cells. *Nat. Commun.* **2024**, *15*, 4403.

(19) Zhu, C.; Huang, K.; Siepser, N. P.; Baker, L. A. Scanning Ion Conductance Microscopy. *Chem. Rev.* **2020**, 121, 11726-11768

(20) Hansma, P. K.; Drake, B.; Marti, O.; Gould, S. A. C.; Prater, C. B. The Scanning Ion-Conductance Microscope. *Science* **1989**, *243*, 641–643.

(21) Siwy, Z. S. Ion-Current Rectification in Nanopores and Nanotubes with Broken Symmetry. *Adv Funct. Mater.* **2006**, *16*, 735–746.

(22) Wei, C.; Bard, A. J.; Feldberg, S. W. Current Rectification at Quartz Nanopipet Electrodes. *Anal. Chem.* **1997**, *69*, 4627–4633.

(23) White, H. S.; Bund, A. Ion Current Rectification at Nanopores in Glass Membranes. *Langmuir* **2008**, *24*, 2212–2218.

(24) Parks, G. A. The Isoelectric Points of Solid Oxides, Solid Hydroxides, and Aqueous Hydroxo Complex Systems. *Chem. Rev.* **1965**, *65*, 177–198.

(25) Kim, S. J.; Wang, Y.-C.; Lee, J. H.; Jang, H.; Han, J. Concentration Polarization and Nonlinear Electrokinetic Flow near a Nanofluidic Channel. *Phys. Rev. Lett.* **2007**, *99*, 44501.

(26) Li, D. *Encyclopedia of Microfluidics and Nanofluidics*; Springer Science & Business Media, 2008.

(27) Yusko, E. C.; An, R.; Mayer, M. Electroosmotic Flow Can Generate Ion Current Rectification in Nano- and Micropores. *ACS Nano* **2010**, *4*, 477–487.

(28) Haywood, D. G.; Harms, Z. D.; Jacobson, S. C. Electroosmotic Flow in Nanofluidic Channels. *Anal. Chem.* **2014**, *86*, 11174–11180.

(29) Ai, Y.; Zhang, M.; Joo, S. W.; Cheney, M. A.; Qian, S. Effects of Electroosmotic Flow on Ionic Current Rectification in Conical Nanopores. *J. Phys. Chem. C* **2010**, *114*, 3883–3890.

(30) Qiu, Y.; Siwy, Z. S.; Wanunu, M. Abnormal Ionic-Current Rectification Caused by Reversed Electroosmotic Flow under Viscosity Gradients across Thin Nanopores. *Anal. Chem.* **2019**, *91*, 996–1004.

(31) Sa, N.; Baker, L. A. Rectification of Nanopores at Surfaces. *J. Am. Chem. Soc.* **2011**, *133*, 10398–10401.

(32) Powell, M. R.; Sa, N.; Davenport, M.; Healy, K.; Vlassiouk, I.; Létant, S. E.; Baker, L. A.; Siwy, Z. S. Noise Properties of Rectifying Nanopores. *J. Phys. Chem. C* **2011**, *115*, 8775–8783.

(33) Stanley, J.; Pourmand, N. Nanopipettes—The Past and the Present. *APL Mater.* **2020**, *8*, 100902.

(34) Anderson, B. N.; Muthukumar, M.; Meller, A. PH Tuning of DNA Translocation Time through Organically Functionalized Nanopores. *ACS Nano* **2013**, *7*, 1408–1414.

(35) Kowalczyk, S. W.; Wells, D. B.; Aksimentiev, A.; Dekker, C. Slowing down DNA Translocation through a Nanopore in Lithium Chloride. *Nano Lett.* **2012**, *12*, 1038–1044.

(36) Umehara, S.; Pourmand, N.; Webb, C. D.; Davis, R. W.; Yasuda, K.; Karhanek, M. Current Rectification with Poly-l-Lysine-Coated Quartz Nanopipettes. *Nano Lett.* **2006**, *6*, 2486–2492.

(37) Zhang, S.; Yin, X.; Li, M.; Zhang, X.; Zhang, X.; Qin, X.; Zhu, Z.; Yang, S.; Shao, Y. Ionic Current Behaviors of Dual Nano- and Micropipettes. *Anal. Chem.* **2018**, *90*, 8592–8599.

(38) Vilozny, B.; Actis, P.; Seger, R. A.; Vallmajo-Martin, Q.; Pourmand, N. Reversible Cation Response with a Protein-Modified Nanopipette. *Anal. Chem.* **2011**, *83*, 6121–6126.

(39) Qian, R.; Wu, M.; Yang, Z.; Wu, Y.; Guo, W.; Zhou, Z.; Wang, X.; Li, D.; Lu, Y. Rectifying Artificial Nanochannels with Multiple Interconvertible Permeability States. *Nat. Commun.* **2024**, *15*, 2051.

(40) Bandara, Y. M. N. D. Y.; Freedman, K. J. Lithium Chloride Effects Field-Induced Protein Unfolding and the Transport Energetics Inside a Nanopipette. *J. Am. Chem. Soc.* **2024**, *146*, 3171–3185.

(41) Cao, L.; Guo, W.; Wang, Y.; Jiang, L. Concentration-Gradient-Dependent Ion Current Rectification in Charged Conical Nanopores. *Langmuir* **2012**, *28*, 2194–2199.

(42) Cheng, L.-J.; Guo, L. J. Rectified Ion Transport through Concentration Gradient in Homogeneous Silica Nanochannels. *Nano Lett.* **2007**, *7*, 3165–3171.

(43) Perry, D.; Page, A.; Chen, B.; Frenguelli, B. G.; Unwin, P. R. Differential-Concentration Scanning Ion Conductance Microscopy. *Anal. Chem.* **2017**, *89*, 12458–12465.

(44) Chau, C. C.; Radford, S. E.; Hewitt, E. W.; Actis, P. Macromolecular Crowding Enhances the Detection of DNA and Proteins by a Solid-State Nanopore. *Nano Lett.* **2020**, *20*, 5553–5561.

(45) Chau, C. C.; Hewitt, E. W.; Actis, P. The Role of Macromolecular Crowding in Single-Entity Electrochemistry: Friend or Foe? *Curr. Opin. Electrochem.* **2021**, *25*, 100654.

(46) Marcuccio, F.; Soulias, D.; Chau, C. C. C.; Radford, S. E.; Hewitt, E.; Actis, P.; Edwards, M. A. Mechanistic Study of the Conductance and Enhanced Single-Molecule Detection in a Polymer–Electrolyte Nanopore. *ACS Nanoscience Au* **2023**, 3, 172-181.

(47) Rabinowitz, J.; Edwards, M. A.; Whittier, E.; Jayant, K.; Shepard, K. L. Nanoscale Fluid Vortices and Nonlinear Electroosmotic Flow Drive Ion Current Rectification in the Presence of Concentration Gradients. *J. Phys. Chem. A* **2019**, *123*, 8285–8293.

(48) Jubin, L.; Poggioli, A.; Siria, A.; Bocquet, L. Dramatic Pressure-Sensitive Ion Conduction in Conical Nanopores. *Proc. Natl. Acad. Sci. U. S. A.* **2018**, *115*, 4063–4068.

(49) Calander, N. Analyte Concentration at the Tip of a Nanopipette. *Anal. Chem.* **2009**, *81*, 8347–8353.

(50) Perry, D.; Momotenko, D.; Lazenby, R. A.; Kang, M.; Unwin, P. R. Characterization of Nanopipettes. *Anal. Chem.* **2016**, *88*, 5523–5530.

(51) Clarke, R. W.; Zhukov, A.; Richards, O.; Johnson, N.; Ostanin, V.; Klenerman, D. Pipette-Surface Interaction: Current Enhancement and Intrinsic Force. *J. Am. Chem. Soc.* **2013**, *135*, 322–329

(52) Teahan, J.; Perry, D.; Chen, B.; McPherson, I. J.; Meloni, G. N.; Unwin, P. R. Scanning Ion Conductance Microscopy: Surface Charge Effects on Electroosmotic Flow Delivery from a Nanopipette. *Anal. Chem.* **2021**, *93*, 12281–12288.

(53) Tao, Z.; Cummings, P. T. Molecular Dynamics Simulation of Inorganic Ions in PEO Aqueous Solution. *Mol. Simul.* **2007**, *33*, 1255–1260.

(54) Weisel, J. W. Fibrinogen and Fibrin. In *Advances in Protein Chemistry*; Academic Press, 2005; Vol. 70, pp 247–299.

(55) Rosentsvit, L.; Wang, W.; Schiffbauer, J.; Chang, H.-C.; Yossifon, G. Ion Current Rectification in Funnel-Shaped Nanochannels: Hysteresis and Inversion Effects. *J. Chem. Phys.* **2015**, *143*, 224706.

(56) Brown, W.; Li, Y.; Yang, R.; Wang, D.; Kvetny, M.; Zheng, H.; Wang, G. Deconvolution of Electroosmotic Flow in Hysteresis Ion Transport through Single Asymmetric Nanopipettes. *Chem. Sci.* **2020**, *11*, 5950–5958.

(57) Ma, Y.; Wang, D. Revealing Electrical Double-Layer Potential of Substrates by Hysteresis Ion Transport in Scanning Ion Conductance Microscopy. *Anal. Chem.* **2021**, *93*, 15821–15825.

(58) Wang, D.; Kvetny, M.; Liu, J.; Brown, W.; Li, Y.; Wang, G. Transmembrane Potential across Single Conical Nanopores and Resulting Memristive and Memcapacitive Ion Transport. *J. Am. Chem. Soc.* **2012**, *134*, 3651–3654.

(59) Sánchez, D.; Anand, U.; Gorelik, J.; Benham, C. D.; Bountra, C.; Lab, M.; Klenerman, D.; Birch, R.; Anand, P.; Korchev, Y. Localized and Non-Contact Mechanical Stimulation of Dorsal Root Ganglion Sensory Neurons Using Scanning Ion Conductance Microscopy. *J. Neurosci. Methods* **2007**, *159*, 26–34.

(60) Meister, A.; Gabi, M.; Behr, P.; Studer, P.; Vörös, J.; Niedermann, P.; Bitterli, J.; Polesel-Maris, J.; Liley, M.; Heinzelmann, H. FluidFM: Combining Atomic Force Microscopy and Nanofluidics in a Universal Liquid Delivery System for Single Cell Applications and Beyond. *Nano Lett.* **2009**, *9*, 2501–2507.

(61) Møller Sønderskov, S.; Hyldgaard Klausen, L.; Amland Skaanvik, S.; Han, X.; Dong, M. In Situ Surface Charge Density Visualization of Self-Assembled DNA Nanostructures after Ion Exchange. *ChemPhysChem* **2020**, *21*, 1474–1482.

(62) Shevchuk, A. I.; Frolenkov, G. I.; Sánchez, D.; James, P. S.; Freedman, N.; Lab, M. J.; Jones, R.; Klenerman, D.; Korchev, Y. E. Imaging Proteins in Membranes of Living Cells by High-Resolution Scanning Ion Conductance Microscopy. *Angew. Chem., Int. Ed.* **2006**, *45*, 2212–2216.

(63) Hall, J. E. Access Resistance of a Small Circular Pore. *J. Gen. Physiol.* **1975**, *66*, 531–532.

(64) Rheinlaender, J.; Schäffer, T. E. Image Formation, Resolution, and Height Measurement in Scanning Ion Conductance Microscopy. *J. Appl. Phys.* **2009**, *105*, 094905.